Sheffield Hallam University

Photo-Fenton degradation of methylene blue using hematite-enriched slag under visible light

ALI, Ahmed, KHAN, Irfan, ZHANG, Bofan, NOMURA, Kiyoshi, HOMONNAY, Zoltan, KUZMANN, Erno, SCRIMSHIRE, Alex, BINGHAM, Paul <http://orcid.org/0000-0001-6017-0798>, KREHULA, Stjepko, MUSIC, Svetozar, AKIYAMA, Kazuhiko and KUBUKI, Shiro

Published version

Copyright and re-use policy

1 # Title page

2 **Names of the authors:**

3 Ahmed S. Ali[1], Irfan Khan[1], Bofan Zhang[1], Kiyoshi Nomura[1], Zoltan Homonnay[2], Erno
4 Kuzmann[2], Alex Scrimshire[3], Paul A Bingham[3], Stjepko Krehula[4], Svetozar Musić[4],
5 Kazuhiko Akiyama[1], Shiro Kubuki[1]

6 **Title:** Photo-Fenton degradation of methylene blue using hematite-enriched slag under
7 visible light

8 **Affiliations and addresses of the authors:**

9 [1] Department of Chemistry, Graduate School of Science and Engineering, Tokyo
10 Metropolitan University, 1-1 Minami-Osawa, Hachi-Oji, Tokyo 192-0397, Japan

11 [2] Institute of Chemistry, Eötvös Loránd University, Pázmány P. s. 1/A, Budapest, 1117,
12 Hungary

13 [3] Materials and Engineering Research Institute, Faculty of Science, Technology and Arts,
14 Sheffield Hallam University, Howard Street, Sheffield S1 1WB, UK

15 [4] Division of Materials Chemistry, Ruđer Bosković Institute, Bijenička c. 54, 10000
16 Zagreb, Croatia

17 **E-mail address of the corresponding author:** Balasfora2000@yahoo.com

18
19
20

21

22

23 **Photo-Fenton degradation of methylene blue using hematite-**
24 **enriched slag under visible light**

25 Ahmed S. Ali[1], Irfan Khan[1], Bofan Zhang[1], Kiyoshi Nomura[1], Zoltan Homonnay[2], Erno
26 Kuzmann[2], Alex Scrimshire[3], Paul A Bingham[3], Stjepko Krehula[4], Svetozar Musić[4],
27 Kazuhiko Akiyama[1], Shiro Kubuki[1]

28

29 *[1] Department of Chemistry, Graduate School of Science and Engineering, Tokyo*
30 *Metropolitan University, 1-1 Minami-Osawa, Hachi-Oji, Tokyo 192-0397, Japan*

31 *[2] Institute of Chemistry, Eötvös Loránd University, Pázmány P. s. 1/A, Budapest, 1117,*
32 *Hungary*

33 *[3] Materials and Engineering Research Institute, Faculty of Science, Technology and Arts,*
34 *Sheffield Hallam University, Howard Street, Sheffield S1 1WB, UK*

35 *[4] Division of Materials Chemistry, Ruđer Bosković Institute, Bijenička c. 54, 10000*
36 *Zagreb, Croatia*

37 **Abstract:**

38 This study aims to find a suitable method to transform the amorphous iron oxides
39 obtained from the incineration of combustible waste slag (CWS) into hematite. The
40 resulting samples were utilized as heterogeneous photocatalysts for the photo-Fenton
41 degradation of methylene blue (MB) aqueous solution. A good correlation was found
42 between the MB degradation and the amount of hematite phase as confirmed by XRD
43 and Mössbauer measurements. The largest rate constant (k) was $(4.1 \pm 0.08) \times 10^{-2}$ min^{-1}
44 for MB decomposition under visible-light for the sample N5-50-800. The results are
45 promising for both low-cost photocatalysts and recycling of combustible waste slags.
46
47
48

49 **Article highlights**

50 • A facile method for slag management into photocatalyst is presented
51 • The key component for degradation was the formation of hematite after heat-
52 treatment
53 • Hematite was confirmed using XRD and Mössbauer techniques
54

55 **Keywords** visible-light activated photocatalytic effect; photo-Fenton reaction; slag;

56 Hematite iron oxide; ^{57}Fe-Mössbauer spectroscopy

57

1. Introduction

59 Among many problems in our world today, two major problems grab the attention of
60 scientists and the public alike: combustible wastes, leading to scarcity of landfill and need
61 to find new recycling and circular economy approaches; and wastewater pollution. With
62 an increasing the world population, these two problems are becoming increasingly
63 serious unless more effective steps are taken [1].

64 For combustible wastes, many countries have established waste incineration or
65 waste-to-energy (WTE) plants to meet the lack of landfill whilst generating useful
66 energy, although the by-products from such processes (ashes and slags) can themselves
67 present both hazards and opportunities [2].

68 There are predominantly two types of slag; firstly, industrial slags which are
69 produced during ferrous and non-ferrous smelting processes. The smelting of copper,
70 lead and bauxite in non-ferrous smelting is designed to remove the iron and silica that
71 often occurs with those ores and separates them as iron-silicate-based slags [3]. On the
72 other hand, ferrous smelting in steel mills is designed to minimize iron loss so these slags
73 mainly consist of oxides of calcium, silicon, magnesium and aluminium. Secondly, there
74 are combustible waste slags (CWS) such as those produced by combustible waste
75 incineration and waste-to-energy (WTE) plants. Such wastes are incinerated at
76 temperatures of ca. 800°C, which reduces the volume to 1/20 of its original volume [4].

77   The compositions of CWS are similar to iron-containing silicate glasses, for which

78   the photocatalytic effect has previously been observed [5]. To date, CWS is used in civil

79   engineering works as a low-value base material or aggregate for the construction of roads

80   and concretes so new applications and new opportunities for valorization and recycling of

81   CWS is essential from both economic and environmental perspectives.

82   For wastewater, several techniques have been applied for the treatment of wastewater

83   effluents. Among these, photocatalysis is one of the most environmentally friendly

84   approaches. The most commonly-applied photocatalyst is TiO_2, which shows

85   photocatalytic activity under UV light due to its wide bandgap of 3.2 eV [6]. This wide

86   bandgap limits the practical uses of TiO_2 as UV light is only available from solar

87   irradiation as a small percentage, ca. 5%, compared to visible light, ca. 40% [7]. Iron

88   oxides, mainly hematite (Fe_2O_3) are promising alternatives due to their lower bandgap

89   around 2.3 eV, low cost, chemical stability and comparatively environmentally friendly

90   nature. Moreover, applying the Fenton reaction and the light-accelerated Fenton reaction,

91   commonly known as the photo-Fenton reaction, provides an added value for using iron

92   oxides as photocatalysts [8].

93   Iida et al. [9] reported that iron alumino-silicate glass,

94    $15Na_2O \cdot 15CaO \cdot 40Fe_2O_3 \cdot 11Al_2O_3 \cdot 19SiO_2$ (weight %), which has a similar composition

95   to CWS, showed a photocatalytic effect after heat treatment at 1000 °C for 100 min, with

96   a k (pseudo-first-order rate constant) of 9.26×10^{-3} min^{-1} for MB degradation. Ishikawa

97   et al. [5] reported that heat treatment of waste slag recycled glass-ceramics (WSRG) with

98   additional Fe_2O_3 content of 10, 30 and 50 mass% decomposed MB aqueous solution

99   with first-order rate constants (k) of 2.6, 2.3 and 2.7×10^{-3} min^{-1}, respectively, under

100   visible light irradiation. The degradation was related to the precipitated amount of α-

101   Fe_2O_3 nanoparticles. Khan et al. [10] also prepared iron-containing aluminosilicate glass

102   by a sol-gel method, which provided a k value of 8.61×10^{-2} min^{-1} in the photo-Fenton

103   degradation of MB, where the amount of precipitated hematite was increased by the

104   introduction of Al_2O_3.

105   In our previous work [11], we succeeded in preparing glass and glass-ceramics from

106   CWS by melt-quenching, obtaining k values of up to 2.2×10^{-2} min^{-1} by melting the slag

107   at 1400 °C, then subsequently heat treating it at 800 °C for 100 min. Here we aim to

108 enhance the results achieved by melt quenching by introducing a facile method for using

109 DSW as a photocatalytic material by treating as-collected DSW with HNO_3 and applying

110 the photo-Fenton reaction under visible light irradiation. The proposed method depends

111 on treating as-collected CWS with nitric acid at room temperature, which could further

112 reduce costs since no high preparation temperatures are required.

113   Reacting nitric acid with CWS compositions, which are mainly metal oxides, will

114 release the metals from the slag matrix in the form of nitrate salts. Iron oxide, Fe_2O_3, as

115 one of these oxides, will convert to iron nitrate which decomposes at high temperatures,

116 through a series of reactions, to form hematite, α-Fe_2O_3 [12], one of the iron oxides used

117 as a visible-light photocatalyst. If some levels of $Fe(NO_3)_3$ persist after heat treatment, it

118 will increase the degradation [13]. There is little literature concerning the acid treatment

119 of CWS. Most related studies have used acid treatment for metals recovery from smelting

120 slags or for neutralizing the acid by adding basic slags. For example, Akcil et al. [14]

121 used nitric acid for the recovery of rare earth metals and production of precipitated silicon

122 dioxide from phosphorus slag which contains inorganic oxides similar to CWS. They

123 used concentrated nitric acid (7.0 – 7.5 M) and slag to acid ratio S: L = 1.0:2.6 at a

124 temperature of 90 °C for 1 hour. Nitric acid was also used for extracting soluble

125 phosphorus from slag with high P_2O_5 content by selective leaching. When nitric acid was

126 used, 66.8% of the solid solution was dissolved [15]. Some researchers have studied

127 photoactivity using metallurgical slag combined with TiO_2, CdO/graphene or other

128 materials, however, some drawbacks exist as some use UV light [16-18], long irradiation

129 times (e.g. 300 min) [19], or low pH (e.g. 3) [20].

130   In this work, the relationship between the visible-light activated catalytic effect and

131 local structure of the slag treated by nitric acid was, for the first time, investigated by

132 [57]Fe-Mössbauer spectroscopy, X-ray diffraction (XRD), transmission electron

133 microscopy (TEM) and optical absorption spectroscopy (UV-Vis).

134

135

136

137

138

2. Experimental Procedures

2.1. Materials

The slag used in this study was collected in July 2018 at the Tamagawa municipal waste combustion plant (Ohta-ku, Tokyo, Japan) according to the agreement between Tamagawa municipal waste combustion plant and faculty of science - Tokyo metropolitan university. Chemical reagents of Nitric acid HNO_3 (13M CAS No. 141-01361), hydrogen peroxide 30% (H_2O_2: CAS No. 081-04215) and methylene blue (MB: $C_{16}H_{18}N_3 S Cl_3 . H_2O$, CAS No. 133-06962) were purchased from Wako, Japan.

2.2. Sample preparation

The as-collected slag was pulverized using an electric agate mortar and the XRF compositional analysis is presented in Table 1. As one of the important parameters affecting the dissolution rates, the ratio of slag/acid is very important [21], several ratios were prepared to study the effect of HNO_3 amount on the structure and photocatalytic ability. One gram of pulverized slag was added to different amounts (20, 10, 5 and 3 ml) of concentrated HNO_3 in a glass beaker and stirred at room temperature. The time required for full dissolution of the slag decreased with the amount of HNO_3. During the dissolution process, black orange fumes were liberated so the whole experiment was performed in an extraction hood. After the dissolution of the slag was complete, a green-coloured solution was obtained. The solution was then directly moved to a dryer at 80 °C in Petri dishes with thickness 2-3 mm, and held for 24 h. Over this period the colour changed from greenish to dark orange, consistent with the change in the iron oxide oxidation state from Fe^{2+} to Fe^{3+}, which was confirmed by [57]Fe Mössbauer measurements as shown in section 3.1.2. The dried samples were pulverized and heat-treated at 1000 °C according to the thermal gravimetric analysis (TG) results (see Fig. 1) at a heating rate of 5 °C/min and the resulting samples are thus denoted N20-1000, N10-1000, N5-1000 and N3-1000. For the samples prepared using dilute HNO_3, the same route was followed by adding additional amounts of distilled water as shown in Table 2. The preparation route is presented in scheme 1. The samples were denoted according to the percentage volume of

168 HNO_3 to the total volume of the solution and the heat treatment temperature. For

169 example, N5-75-800 means that for one gram of slag, the total volume of the solution is 5

170 ml while the HNO_3 volume is 75% and the heat treatment temperature is 800 °C. The

171 sample of 25% HNO_3 content did not fully dissolve so we obtained two samples, N5-75

172 and N5-50, which were heat-treated at 800 and 1000 °C.

173

2.3.   Characterization techniques

175   Sample structure before and after heat treatment were characterized by [57]Fe

176 Mössbauer spectroscopy, X-ray diffractometry (XRD), Scanning electron microscopy

177 (SEM), Transmission electron microscopy (TEM) and the Brunauer-Emmett-Teller

178 (BET) specific surface area analysis. [57]Fe Mössbauer spectra were measured using a

179 constant acceleration spectrometer. A source of 925 MBq [57]Co (Rh) was attached to an

180 MVT-1000 transducer connected to an MDU-1200 drive unit. The drive unit was

181 connected to a DFG-1200 digital function generator with 1200 channels. Transmitted γ-

182 rays were detected by a proportional counter. The signals were amplified by an ORTEC

183 142 preamplifier. The applied voltage (2 kV) was obtained by using an ORTEC 556 High

184 voltage–power supply, and an ORTEC 570 amplifier. The amplified signals were

185 monitored with a PC via an ORTEC EASYMSC. Samples with weight = 40 mg were

186 homogeneously dispersed in a circular sample holder with 10 mm diameter; inserted into

187 the spectrometer, and measured until the total counts collected were greater than 10^6.

188 Isomer shifts are given relative to α-Fe, which was measured as a reference. The

189 Mösswinn 3.0i XP software was used to analyze the obtained spectra. XRD patterns were

190 recorded using a RINT TTR3, Rigaku diffractometer between 2θ of 10° to 80°, with

191 precision and scan rates of 0.02 and 5°/ min, respectively. Cu-Kα X-rays ($\lambda = 0.1541$ nm)

192 were generated at 50 kV and 300 mA, and monochromated. SEM images were taken by

193 Keyence VE 9800 with the applied voltage of 2 kV, and magnification of 2000x. TEM

194 images were obtained using a JEM-3200FS Field Emission Energy Filter Electron

195 Microscope. The Brunauer-Emmett-Teller (BET) specific surface area was estimated

196 from N_2 isotherms obtained using a BELSORP mini II (BEL Japan, Osaka, Japan) at 77

197 K. The analyzed samples were evacuated at 573 K for 3 h before each measurement.

198

2.4. Photo-Fenton Reaction

200   For the evaluation of photocatalytic properties, we used 40 mg of pulverized sample

201 and 10 mL of methylene blue aqueous solution (MB_{aq}) with an initial concentration of

202 20 μmol L^{-1}. Additional amounts of hydrogen peroxide (9.79 M) (Wako: 081-04215 30%

203 mass/mass) was added to the MB solution. UV–Vis optical absorption spectra of the MB

204 solution before and after the photocatalytic reaction test were measured from the

205 absorbance of the peak at 665 nm, using a GENESYS™ 10S UV-Vis spectrophotometer.

206 The light was emitted by a metal-halide lamp with output wavelengths from 420 to

207 750 nm, an output power of 100 W and an intensity of 6 mW cm^{-2}, with the distance

208 between the sample and the light source maintained at 20 cm, and a UV filter was used.

209 All samples were also measured in the dark to investigate the effect of adsorption as a

210 control. All measurements were performed at room temperature.

211

3. Results and discussion

3.1. Structural characterization

3.1.1 XRD

215   Figure 2(a) shows the XRD patterns for the samples dissolved in concentrated HNO_3

216 heat-treated at 1000 °C for 100 min. The samples N20, N10 and N5 show crystalline

217 peaks ascribed to hematite (Fe_2O_3, PDF No. 01-089-0598), gehlenite (Ca_2Al (Al Si) O_7,

218 PDF No. 01-089-5917) and esseneite ($CaFe_{0.6}Al_{1.34}Si_{1.08}O_6$, PDF No. 01-084-1206). The

219 sample N3 does not evidence peaks related to hematite but shows peaks consistent with

220 gehlenite and esseneite, with the same PDF numbers previously mentioned. This sample

221 also produces diffraction peaks attributed to Andradite ($Ca_3Fe_2O_{12}Si_3$, PDF No. 01-084-

222 1206). The intensity of hematite peaks decreases, with decreasing HNO_3 addition from 20

223 to 5 ml for the samples N20 to N5, respectively. These results indicate that the amount of

224 HNO_3 has a large impact on the development of the hematite phase obtained from heat-

225 treatment. Since hematite is known as a visible light photocatalyst, it was expected that

226 the sample N20 would produce the highest MB_{aq} degradation values due to the existence

227   of hematite as the most prominent phase. It was also expected that the MB_{aq} degradation

228   of the samples N10, N5 and N3 would decrease gradually due to the gradual decrease in

229   hematite content. It should be noted that in our previous work [11], we could not detect

230   any XRD peaks related to hematite in the slag after melting at 1400 °C and heat-

231   treatment at 800 °C for 100 min unless Fe_2O_3 additions were made to increase the Fe_2O_3

232   content of the resulting material to 50%. Figure 2(c) shows the XRD pattern of the slag

233   (same slag used in this study), melted at 1400 °C and heat-treated at 800 °C for 100 min.

234   The identified phases are iron silicon oxide ($Fe_{2.95}Si_{0.05}O_4$, PDF No. 00-052-1140) and

235   calcium silicate (Ca_2SiO_4, PDF No. 00-024-0234). This means that dissolving the slag in

236   HNO_3 can produce hematite without the requirement for additional Fe_2O_3, leading to

237   better degradation results and simpler production.

238   Figure 2(b) shows the XRD patterns for the samples dissolved in dilute HNO_3 (75

239   and 50%) after heat treatment at 800 and 1000 °C for 100 min, respectively. Clear

240   diffraction peaks can be detected for gehlenite (Ca_2Al (Al, Si) O_7, PDF No. 01-089-

241   5917), hematite (Fe_2O_3, PDF No. 01-089-0596) and andradite (Ca_3Fe_2 $(SiO_4)_3$, PDF No.

242   01-084-1935) for all samples. Heat treatment at 1000 °C for both N5-75 and N5-50

243   samples increased their crystallinity as demonstrated by the narrower diffraction peaks

244   compared to those obtained in the corresponding samples heat-treated at 800 °C,

245   suggesting that the crystallite size increased as the temperature increased, which is also

246   reflected in the measured surface area. Also, the intensity of hematite peaks decreased

247   while the intensity of gehlenite peaks increased for heat treatment at 1000 °C compared

248   to 800 °C. It is thus concluded that HNO_3 concentration plays a major role in controlling

249   the obtained phases while heat treatment temperature affects the phase distribution and

250   the crystallite size. These results are consistent with that obtained from Mössbauer

251   spectra.

252

253   **3.1.2 Mössbauer Spectroscopy**

254   **3.1.2.1 Mössbauer spectroscopy of slag dissolved in concentrated HNO_3**

255   The as-collected slag spectra and fitted data, in Fig. 4(c) and Table 3, show two

256   paramagnetic doublets with δ = 1.01 $\pm$ 0.01 mm s^{-1} and 0.48 $\pm$ 0.06 mm s^{-1} related to

257    $Fe^{II} O_h$ and $Fe^{III} O_h$, respectively. The spectra and parameters for all samples prepared

258   using concentrated HNO_3 after heat treatment at 1000 °C for 100 min are shown in Fig. 3

259   and Table 3, respectively. The spectra of the samples N20, N10 and N5 exhibit two

260   doublets related to Fe^{III} and one sextet related to hematite. The sample N3 shows only

261   two doublets with $\delta = 0.29 \pm 0.01$ and 0.38 ± 0.01 mm s^{-1} related to $Fe^{III} T_d$ and $Fe^{III} O_h$,

262   respectively. These results show that Fe^{II} in the slag was oxidized to Fe^{III} upon dissolution

263   in HNO_3 and drying, while hematite can be formed by heat treatment. On the other hand,

264   the spectra and fitted parameters for the sample prepared by melt-quenching after heat

265   treatment at 800 °C for 100 min, shown in Fig. 4(c) and Table 3, show two doublets with

266    $\delta = 0.36 \pm 0.01$ and 0.34 ± 0.01 mm s^{-1}, related to $Fe^{III} O_h$, which is similar to

267    $\delta = 0.38 \pm 0.04$ mm s^{-1} obtained for the sample prepared by melt-quenching reported in

268   our previous paper [11]. The detection of hematite in the dissolved slag following heat

269   treatment is interesting behaviour compared to melt-quenching, although both samples

270   have the same total iron content. In our previous paper [11], where the samples were

271   prepared using melt-quenching, hematite was detected by RT-Mössbauer only for the

272   sample containing 50% Fe_2O_3. The existence of hematite in the dissolved slag was found

273   to be effective for MB degradation, as will be discussed in degradation measurements

274   section. This demonstrates the advantage of dissolving slag in HNO_3 over melt-

275   quenching, to prepare an effective, low-cost photocatalyst. It is noticed that the hematite

276   absorption peak decreases as the amount of HNO_3 decreased, where it was 33, 29 and

277   20% for N20, N10 and N5, respectively. This may be due to the lower amount of HNO_3

278   resulting in the incomplete dissolution of iron oxide in slag. As a result, a lower amount

279   of iron nitrate may be formed, and consequently, the hematite, which results from thermal

280   decomposition of iron nitrate, was decreased. This can be seen in the case of sample N3,

281   for which no hematite was detected for the above-mentioned reason. The Mössbauer

282   results are consistent with the XRD results.

283

284   **3.1.2.2 Mössbauer spectroscopy of slag dissolved in diluted HNO_3**

285   The spectra and fitted parameters for the samples dissolved in dilute HNO_3 (75 and

286   50%) before and after heat treatment at 800 and 1000 °C for 100 min are shown in Fig.

287   4(a), (b) and Table 4, respectively. Using diluted HNO_3 (with HNO_3 of 75%) resulted in

288   hematite content with absorption peaks of 38 and 40% for the samples N5-75-1000 and

289   N5-75-800 °C, respectively. Further decrease in HNO_3 concentration to 50% resulted in

290   more hematite with absorption peaks of 33 and 50% for the samples N5-50-1000 and N5-

291   50-800 °C, respectively. Compared to the hematite content (20%) in the case of the

292   sample produced using concentrated HNO_3 (N5-1000), it can be observed that more

293   dilute HNO_3 is more effective for obtaining high hematite contents in the final materials,

294   which can enhance the photocatalyst performance. This can be explained by the

295   hydrolysis being affected by the ratio of water in the solution. Before heat treatment, both

296   samples show two doublets related to $Fe^{III} O_h$ with $\delta = 0.37 \pm 0.02$ and 0.57 ± 0.04

297   mm s^{-1} for N5-75, $\delta = 0.36 \pm 0.01$ and 0.39 ± 0.05 mm s^{-1} for N5-50, respectively,

298   indicating the oxidation of Fe^{II} in the slag to Fe^{III} after drying, however, heat treatment is

299   required for the formation of hematite. To obtain more investigation about the effect of

300   heat treatment temperature on the obtained hematite, the sample N5-50 was heat-treated

301   at 600 °C for 100 min. From Mössbauer measurements shown in Fig 4(c) and Table 4,

302   only two doublets were obtained with $\delta = 0.32 \pm 0.01$ and 0.35 ± 0.02 mm s^{-1} and

303   assigned as $Fe^{III} T_d$ and $Fe^{III} O_h$, respectively, with no hematite detected. These results

304   show that, of those temperatures studied here, the most effective heat treatment

305   temperature to obtain hematite is 800 °C.

306

307   ### 3.1.3. Morphology

308   Fig. 5 (A, B) show the SEM and TEM images of the samples N5-75 and N5-50 heat-

309   treated at 800 and 1000 °C, respectively. From SEM images, all samples show uneven

310   surfaces with different sizes and morphologies. The size and morphology are smaller,

311   more porous and uniform in the case of lower heat-treated samples N5-75-800 and N5-

312   50-800 compared to higher heat-treated samples N5-75-1000 and N5-50-1000. The

313   average aggregate' sizes are 4.2, 5.4, 3.9, and 4.4 μm for N5-75-800, N5-75-1000, N5-50-

314   800 and N5-50-1000, respectively. Average aggregate' sizes are lower in the case of

315   lower heat-treatment which is an advantage for using these samples in practical

316   applications. The TEM images give a more clear analysis of these samples, for which the

317 particle size for N5-75-800 varies from 5 to 9 nm, having the smallest particle size among

318 all samples studied. For sample N5-75-1000, the particle size has grown slightly to

319 approximately 12 nm. The sample N5-50-800 has particles with a size approximately 21

320 nm while sample N5-50-1000 exhibits particles with sizes varies from 15 to 24 nm.

321 These larger particle sizes for samples heat-treated at 1000 °C are consistent with their

322 higher heat treatment temperatures.

323

3.2.   Photocatalytic properties

3.2.1. Photo-Fenton reaction for the concentrated HNO$_3$ treated samples

327 The results of MB degradation under the photo-Fenton reaction of the heat-treated

328 samples N20, N10, N5 and N3 (see Fig. 6) show that the degradation and *k* values

329 increase with the amount of HNO$_3$ used for dissolving the slag. This trend can be

330 explained by considering the structural characterization from both XRD and Mössbauer

331 spectroscopy; it is correlated with the amount of hematite in the sample. The apparent *k*

332 values for the samples N20, N10, N5 and N3 were $(8.1 \pm 0.2, 5.0 \pm 0.2, 3.0 \pm 0.1$ and

333 $1.4 \pm 0.1) \times 10^{-2}$ min^{-1} after 60 min of irradiation where the hematite contents were 33%,

334 29%, 20% and zero, respectively. To clarify the greater effectiveness of this method over

335 melt-quenching, another sample was prepared by melt-quenching using the same

336 collected slag, and then heat-treated at 800 °C for 100 min. The MB test for this sample

337 resulted in a *k* value of $2.2 \pm 0.1 \times 10^{-2}$ min^{-1} after 3h of irradiation. These results show

338 that the acid dissolution and heat treatment method resulted in cost-effective visible light

339 photocatalysts also reducing the time required for the MB degradation from 3h to 1h. The

340 degradation of the blank sample (without catalyst) and dark samples (measured in the

341 dark) have small *k* values of $(0.25 \pm 0.01, 0.28 \pm 0.01, 0.25 \pm 0.01, 0.21 \pm 0.01,$ and

342 $0.10 \pm 0.01) \times 10^{-2}$ min^{-1}, respectively, which means that the degradation is due mainly to

343 photoactivity rather than photolysis or adsorption. The advantage of the photo-Fenton

344 reaction over photoactivity can be clarified by measuring all samples under the same

345 conditions without applying the photo-Fenton reaction. The *k* values for samples N20,

346 N10, N5 and N3 were $(1.32 \pm 0.03, 1.01 \pm 0.02, 0.48 \pm 0.01$ and $0.3 \pm 0.01) \times 10^{-2}$ min^{-1},

347 respectively, which are far smaller compared to k values from the photo-Fenton reaction,

348 however, it has the same trend in variation of k as a function of hematite content.

349

350

351 3.2.2. Photo-Fenton reaction for the diluted HNO$_3$ treated samples

352 We aimed to prepare a cost-effective catalyst so the k / acid ratio was calculated to

353 choose the most practical sample. From these results, shown in Fig. 6 inset, sample N5

354 was chosen since it provided the highest k / acid ratio. The amount of HNO$_3$ was diluted

355 with distilled water to 75, 50 and 25%. The slag could not be fully dissolved at the low

356 HNO$_3$ concentration of 25% so two samples denoted as N5-75 and N5-50 were obtained

357 for the corresponding HNO$_3$ concentrations of 75 and 50%, respectively. Both samples

358 were heat-treated at 1000 and 800 °C according to the TG results (see Fig. 1) and denoted

359 as samples N5-75-1000, N5-75-800, N5-50-1000 and N5-50-800, respectively. The

360 photo-Fenton measurements for these samples are shown in Fig. 7, and the results can be

361 summarized as follows:

362 Firstly, the k values in the case of samples N5-75-1000 and N5-75-800 were

363 $(3.9 \pm 0.1$ and $4.5 \pm 0.1) \times 10^{-2}$ min^{-1}, respectively, while for samples N5-50-1000 and

364 N5-50-800 it was $(3.4 \pm 0.1$ and $4.1 \pm 0.1) \times 10^{-2}$ min^{-1}, respectively. The higher k values

365 in the case of higher acid content indicate that the slag / acid ratio plays a major role in

366 the effectiveness of the prepared catalyst.

367 Secondly, the results of photo-Fenton reactions are correlated with the hematite

368 content of the sample. The Mössbauer absorption area (Table 4) for sample N5-50-800

369 was detected to be 50%, having a k value of $(4.1 \pm 0.1) \times 10^{-2}$ min^{-1} while absorption area

370 was 33% for sample N5-50-1000 with a lower k value of $(3.9 \pm 0.1) \times 10^{-2}$ min^{-1}. The

371 same trend can be observed for the sample N5-75 although the difference in the

372 absorption area is not large (40% for 800 °C and 38% for 1000 °C) but it is also

373 important to consider the additional doublet for the sample prepared at 800 °C with the

374 octahedral site and absorption area of 10%.

375 Thirdly, for each sample, it can be seen that the lower heat treatment temperature

376 resulted in higher MB degradation. This can be an indication of particle size (and

377   therefore higher surface area) contribution where the particle size is larger in the higher

378   temperature samples. From XRD shown in Fig. 2(a) and (b), it can be observed that both

379   samples N5-75-1000 and N5-50-1000 produce sharp diffraction peaks with narrow full-

380   width, half-maximum (FWHM) line widths compared to XRD patterns for samples N5-

381   75-800 and N5-50-800. Sharp diffraction peaks correspond to larger crystallite size,

382   which is reflected in the surface area, an important parameter for effective photocatalysts.

383   To clarify the contribution of surface area and its relation to MB degradation, the surface

384   areas of these samples were measured. The BET results (Table 5) clearly show that the

385   surface area has a positive correlation with MB degradation, where it is larger in the case

386   of higher HNO_3 content and low heat treatment temperature, (3.64 and 5.38 m^2 / g) for

387   samples N5-75-1000 and N5-75-800 compared to the lower HNO_3 content (2.16 and 2.63

388   m^2 / g) for samples N5-50-1000 and N5-50-800, respectively.

389   Fourthly, the sample prepared by melt-quenching has a *k* value of $(2.2 \pm 0.1) \times 10^{-2}$

390   min^{-1} which is almost half of that for the HNO_3 produced samples. By considering the

391   structural analysis of this sample, it can be seen that it produces only Mössbauer doublets

392   and no hematite sextets, and thus no hematite can be observed by either XRD Fig. 2(c) or

393   Mössbauer spectroscopy Fig. 4(c). This may be the reason for the low *k* value obtained

394   for this sample in addition to the fact that the melt-quenching method results in lower

395   surface area.

396   Fifthly, before heat treatment, the photoactivity of both samples N5-75 and N5-50

397   were measured. It was found that they produce much higher MB degradation than the

398   heat-treated samples, with 88% of MB removal for both samples after only 20 min. Both

399   samples were measured in dark conditions and also provide high MB degradation of 68%

400   and 61% after 20 min for samples N5-75 and N5-50, respectively. These values were

401   mainly due to the effect of adsorption and homogeneous Fenton reaction rather than the

402   photo-Fenton reaction. Iron nitrate salts (present in the samples before heat treatment)

403   accompanied by low pH (due to the presence of HNO_3 which is not completely removed

404   after drying at 80 °C) are a good environment for the homogeneous Fenton reaction. The

405   sample N5-50 was heat-treated at 600 °C for 100 min and shows a lower *k* value of

406    $(1.5 \pm 0.1) \times 10^{-2}$ min^{-1} compared to sample N-5-50-800. By considering the fitted

407   Mössbauer parameters for this sample (Table 4), the spectra are composed of two

408 doublets with δ = (0.35 ± 0.02 and 0.32 ± 0.01) mm s^{-1} assigned as Fe^{III} O_h and Fe^{III} T_d,

409 respectively, where hematite is not detected (lack of sextet), which confirms that hematite

410 plays the major role in the MB degradation and it can be obtained only by heat treatment

411 at 800 °C.

412

413 3.2.3. Parameters affecting MB degradation

414 The sample N5-50-800 has lower acid content and lower heat treatment temperature,

415 hence, it was chosen for further study.

416

417 **a- Effect of H$_2$O$_2$**

418 The oxidation of organic pollutants using Fenton reactions is strongly dependent on

419 the addition of H$_2$O$_2$ because it controls the generation of active radicals. The MB

420 degradation has been studied under a range of H$_2$O$_2$ concentrations (0.1 to 1.6 M); the

421 results are shown in Fig. 8(a). By increasing the H$_2$O$_2$ concentration from 0.1 to 0.35 M

422 the degradation increases from 70.3% to 90.6% removal of MB where more H$_2$O$_2$

423 produces more active radicals [22]. However, excess H$_2$O$_2$ decreases the degradation

424 from 90.6% to 80.8%, mostly because it acts as a scavenger of hydroxyl radicals [22, 23].

425 Also, more H$_2$O$_2$ can generate more $^.$OH, which can be dimerized to form H$_2$O$_2$ so

426 cumulative effects can inhibit the MB degradation. The excess of H$_2$O$_2$ may also

427 encourage the formation of less active hydroperoxyl radicals which can react with

428 hydroxyl radicals to form water [24]. The best-performing H$_2$O$_2$ concentration was found

429 to be 0.35 M, which produced a k value of 4.1×10^{-2} min^{-1}.

430

431 **b- Effect of MB concentration**

432 Dye concentration affects the intensity of light passing through the reaction medium

433 to reach the surface of the photocatalyst. The photodegradation of MB was conducted

434 under initial concentrations of 20, 40 and 60 μM. MB degradation is shown in Fig. 8(b)

435 and displays an inverse relation with the initial concentration, where it was 90.6%, 69.2%

436 and 65.5% for MB of 20, 40 and 60 μM after 60 min of irradiation, respectively. This can

437   be attributed to the decrease in˙OH, radical generation due to the coverage of catalyst

438   active sites by the adsorbed dye [24, 25]. Moreover, the intermediate compounds formed

439   during the degradation process increase with the increase in the initial dye concentration

440   and might consume some active radicals that are supposed to react with the dye

441   molecules [26].

442

443   **c- Effect of catalyst loading**

444   Determining the optimum catalyst loading is essential in photodegradation reactions,

445   since it helps in consequently scaling up the photocatalytic process, thereby affecting the

446   economics of the whole process. This includes the production cost which should be

447   minimized. Not only this but also catalyst recovery after the end of the reaction must be

448   considered. In our case, the prepared catalyst (iron silicate powder) loading was varied

449   from 2 to 24 g L^{-1}. The results of MB degradation measured after 60 min as a function of

450   the catalyst loading are presented in Fig. 8(c). Increase in the MB degradation was

451   observed, from 84.4% for 2 g L^{-1} to 90.6% for 4 g L^{-1}. This increase in degradation is due

452   to the increase in the active surfaces for the same unit volume of MB [24], which will

453   lead to an increase in the absorbed photons and consequently in the generation of˙OH

454   radicals which initiate the reaction [25]. Further increase leads to a decrease in MB

455   degradation from 90.6% for 4 g L^{-1} to 81.8% for 24 g L^{-1}, mostly caused by a reduction in

456   light intensity as the solution opacity increases [27, 28]. It is also possible that at higher

457   catalyst loading, the iron act as a scavenger and reacts with˙OH radicals [24].   The

458   optimum catalyst loading was found to be 4 g L^{-1}.

459

460   **d- Effect of temperature**

461   The reaction temperature is a critical operating parameter. Fig 8(d) shows the

462   influence of the reaction temperature on MB removal. The experiments were performed

463   at four different temperatures, namely, 303K, 313K, 323K, and 333K. It can be seen that

464   with increasing temperature, the rate of the reaction increases from 4.1×10^{-2} min^{-1} at

465   303K to 13.0×10^{-2} min^{-1} at 333K. The increase in temperature increases interaction of

466   the hydroxyl radicals and the dye molecules and the reaction competes more efficiently
467   with electron-hole recombination [11, 28].

468   The activation energy (E_a), estimated using the rate constants (k_t) from the Arrhenius
469   equation [22], were calculated according to Eq. (1)

470

471                          $$\ln k_t = - E_a/RT + \ln A \qquad\qquad (1)$$

472

473   Where k_t is the reaction rate constant as a function of temperature; E_a ($J \cdot mol^{-1}$) is the
474   apparent activation energy; R is the universal gas constant of 8.314 $J \cdot mol^{-1} \cdot L^{-1}$; T (K) is
475   the absolute temperature; A is the Arrhenius pre-exponential factor

476   The apparent activation energy of MB obtained in this study Fig. 8(d) (inset) was
477   31.5 $KJ.mol^{-1}$ which is higher than values obtained from other studies reported by
478   Okamoto [29] for the photodegradation of phenol (10.0 kJ / mole) and by Al-Sayyed [30]
479   for the degradation of 4-chlorophenol (5.4 kJ / mole). The high value obtained in this
480   study suggests that thermal activation is important to accelerate the photo-degradation
481   [31].

482

483   **e-   Effect of pH**

484

485   The pH is considered the main parameter affecting the adsorption/desorption
486   processes due to its impact on the surface charge of the catalyst. This affects the
487   adsorption of reactants and dye molecules on the surface of the catalyst, and desorption
488   of the reaction products back into solution [26]. The effect of the solution pH within the
489   range of 3 to 11 on the degradation efficiency was investigated; the results are presented
490   in Fig. 9. An increase in the degradation efficiency was observed with increasing pH
491   from 3 to 11. At pH 11 the MB degradation is highest at 93.8% in 20 min, while the
492   maximum degradation at lower pH was 32.2% and 80.5 % for pH of 9 after 20 and 60
493   min, respectively. The pH of the solution can enhance the degradation and ensure strong
494   adhesion of dye molecules on the surface of the catalyst. This depends on the nature of

495 the dye (cationic, anionic or neutral). In our case, MB, which is a cationic dye, will be

496 adsorbed more quickly at higher pH and consequently, an increase in the MB degradation

497 rate is expected [25, 26]. The alkaline medium can also facilitate the formation of $^-$OH

498 ions which are responsible for the generation of $^.$OH radicals; this will lead to an increase

499 in photodegradation rate [32]. It was reported that in acidic solutions, the surfaces of

500 photocatalysts are positively charged while they are negatively charged in alkaline

501 solutions [33]. As a result, the efficiency of MB photodegradation is expected to increase

502 with pH, owing to electrostatic interactions between the negative surface and the MB

503 cations.

504 To understand the influence of the solution pH on the Fenton process, the point of

505 zero charge (PZC) of the N-5-50-800 sample was estimated (Inset Fig. 9). The obtained

506 PZC value of 10.6 suggests that the surfaces of the catalyst were negatively charged at

507 pH higher than 10.6, which is ideal for the degradation of the cationic MB due to

508 electrostatic interactions [22]. The high value of PZC explains the rapid increase in the

509 degradation from 32.2% to 93.8% for pH of 11 and 9 after 20 min, respectively.

510

3.2.4. Stability and Recyclability

512 Catalyst recyclability is an increasingly important feature of catalysts for industrial

513 applications. In this study, the reusability of the best-performing sample, N5-50-800, was

514 tested at an initial pH of 11. Fig. 10 illustrates the relationship between MB degradation

515 efficiency and the number of cycles, tested at 20 min of irradiation after 7 successive

516 cycles where the degradation was decreased by only 6.3%. The repeated measurements

517 were carried out by centrifuging the solution followed by removing and replacing it with

518 a new MB solution. No further filtration or drying of the powder was carried out between

519 subsequent experiments, which can further lower the operational cost if the catalyst were

520 applied in a large-scale process.

521

Conclusions

523 A visible light photocatalyst was successfully prepared by dissolving the combustible

524 waste slag in nitric acid. The photocatalytic activity of the prepared samples was found to

obey the pseudo-first-order rate constant, having a *k*-value of $(4.1 \pm 0.1) \times 10^{-2}$ min^{-1} for sample N5-50-800 in the photo-Fenton process. The *k*-value increased to $(1.4 \pm 0.1) \times 10^{-1}$ min^{-1} for the same sample after controlling the initial pH to 11. The sample prepared by the melt-quenching method using the same slag has a maximum *k* value of $(2.2 \pm 0.1) \times 10^{-2}$ min^{-1} under the same conditions, which illustrates the effectiveness of the method used in this study. The obtained results of photocatalytic activity are correlated to the amount of hematite in each sample, as detected by XRD and ^{57}Fe Mössbauer measurements. It was found that the HNO_3 concentration and heat treatment temperature have a large impact on both hematite content and the surface area of the prepared samples and, consequently, on the methylene blue degradation ability. The optimum conditions for practical usage of the samples are using sample N5-50-800 in the photo-Fenton reaction with 0.35 M of H_2O_2, a catalyst (iron silicate powder) loading of 4 g L^{-1}, MB initial concentration 20 μM and initial pH of 11.

CRediT author statement:

Ahmed Salah Ali: Conceptualization, Methodology **Irfan Khan:** Writing-Reviewing and Editing **Bofan Zhang:** Methodology **Kiyoshi Nomura:** Software **Homonnay Zoltan:** Writing-Reviewing and Editing **Erno Kuzmann:** Writing-Orginal draft **Alex Scrimeshire:** Software **Paul Bingham:** Methodology **Stjepko Krehula:** Visualization **Svetozar Music:** Data curation **Kazuhiko Akiyama:** Data curation **Shiro Kubuki:** Supervision.

Declaration on conflict of interests

The authors declare that they have no known competing financial interests or personal relationships that could have appeared to influence the work reported in this paper.

Acknowledgements

554

References

[1] Ferronato N, Torretta V (2019) Waste mismanagement in developing countries: A review of global issues. Int. J. Environ. Res. Public Health 16:1–28

[2] Mary Joseph A, Snellings R, Heede P V d, Matthys S, Belie N.D (2018) The use of municipal solid waste incineration ash in various building materials: A Belgian point of view. Materials 11:1–30

[3] Yildirim I Z, Prezzi M (2011) Chemical, mineralogical and morphological properties of steel slag. Adv. Civ. Eng. 2011:1–13

[4] Perrot J F, Alison Subiantoro A (2018) Municipal waste management strategy review and waste-to-energy potentials in New Zealand. Sustainability 10:1–12

[5] Ishikawa S, Kobzi B, Sunakawa K, Nemeth S, Lengyel A, Kuzmann E, Homonnay Z, Nishida T, Kubuki S (2017) Visible-light activated photocatalytic effect of glass and glass ceramic prepared by recycling waste slag with hematite. Pure Appl. Chem. 89: 535–554

[6] Fujishima A, Honda K (1972) Electrochemical photolysis of water at a semiconductor electrode. Nature 238:37-38

[7] Koehl M, Philipp D, Lenck N, Zundel M (2009) Development and application of a UV light source for PV-module testing. Proc. of SPIE 7412:1–7

[8] Aramyan S, Moussavi M (2017) Advances in Fenton and Fenton Based Oxidation Processes for Industrial Effluent Contaminants Control-A Review. Int. J Environ. Sci. Nat. Res. 2:1–18

[9] Iida Y, Akiyama K, Kobzi B, Sinkó K, Homonnay Z, Kuzmann E, Ristić M, Krehula S, Nishida T, Kubuki S (2015) Structural analysis and visible light-activated photocatalytic activity of iron-containing soda lime aluminosilicate glass. J. Alloys. Comp. 645:1–6

[10] Khan I, Nomura K, Kuzmann E, Homonnay Z, Sinkó K, Ristić M, Krehula S, Musić S, Kubuki S (2020) Photo-Fenton catalytic ability of iron-containing aluminosilicate glass prepared by sol-gel method. J. Alloys. Comp. 816:1–7

583 [11] Ali A S, Nomura K, Homonnay Z, Kuzmann E, Scrimshire A, Bingham P A,
584   Krehula S, Ristić M, Musić S, Kubuki S (2019) The relationship between local
585   structure and photo‑ Fenton catalytic ability of glasses and glass‑ ceramics prepared
586   from Japanese slag. J. Radioanal. Nuc. Chem. 322:751–761

587 [12] Melnikov P, Nascimento V A, Arkhangelsky I V, Zanoni Consolo L Z, de Oliveira L
588   C S (2014) Thermal decomposition mechanism of iron (III) nitrate and
589   characterization of intermediate products by the technique of computerized
590   modeling. J Therm. Anal. Calorim. 115:145–151

591 [13] Machulek A, Quina F, Gozzi F, Silva V, Friedrich L, Moraes J (2012) In: Puzyn T
592   (ed) Organic pollutants ten years after the Stockholm convention—environmental
593   and analytical update, 1st edn. Intechopen, London

594 [14] Akcil A, Karshigina Z B, Bochevskaya Ye G, Abisheva Z S (2018) Conditions of
595   nitric acid treatment of phosphorus slag from REMs recovery and production of
596   precipitated silicon. Metallurgy 2:28–38

597 [15] Du C, Gao X, Ueda S, Kitamura S (2016) Effects of Cooling Rate and Acid on
598   Extracting Soluble Phosphorus from Slag with High P_2O_5 Content by Selective
599   Leaching. ISIJ International 510:1–10

600 [16] Zhang Y, He P. Chen H (2018) A novel CdO/graphene alkali-activated steel slag
601   nanocomposite for photocatalytic degradation of dye wastewater. Ferroelectrics
602   522:1–8

603 [17] Kang L, Zhang Y, Wang L, Zhang L, Zhang K, Liu L (2015) Alkali-Activated steel
604   slag-based besoporous material as a new photocatalyst for degradation of dye from
605   wastewater. Integr. Ferroelectr. 162:8–17

606 [18] Zeynolabedin R, Mahanpoor K (2017) Preparation and characterization of nano-
607   spherical $CoFe_2O_4$ supported on copper slag as a catalyst for photocatalytic
608   degradation of 2-nitrophenol in water. J. Nanostruct. Chem. 7:67–74

609 [19] Salgado S Y A, Pérez A A M, López M S, Zamora R M R (2016) Evaluation of
610   metallurgical slag as a Fenton-type photocatalyst for the degradation of an
611   emerging pulutent: Diclofenac. Catal. Today 266:126–135

612 [20] Gong X, Jia F, Liu R, Ye F, Guan H, Wang R, Guo G (2014) Study on preparation
613 and photocatalytic activity of photocatalyst made from Ti-bearing blast furnace slag.
614 Appl. Mech. Mater. 526:33–39

615 [21] Sun Y, Zhang J, Wang Y, Li Q (2016) Inhibitory Effect of Thioacetamide On CdS
616 Dissolution During Photocatalytic Oxidation of 2,4-Dichlorophenol. Rare Metal
617 Technology 1:87-88

618 [22] Saleh R, Taufik A (2019) Degradation of methylene blue and congo-red dyes using
619 Fenton, photoFenton, sono-Fenton, and sonophoto-Fenton methods in the presence
620 of iron (II,III) oxide/zinc oxide/graphene (Fe_3O_4/ZnO/graphene) composites. Sep.
621 Purif. Technol. 210:563-573

622 [23] Guo S, Zhang G, Wang J (2014) Photo-Fenton degradation of Rhodamine B using
623 Fe_2O_3–Kaolin as heterogeneous catalyst: Characterization, process optimization
624 and mechanism. J. Colloid Interf. Sci. 433:1-8

625 [24] Nasuh N, Ismail S, Hameed H (2016) Activated electric arc furnace slag as an
626 effective and reusable Fenton-like catalyst for the photodegradation of methylene
627 blue and acid blue 29. J. Taiwan Inst. Chem. E. 67:235–243

628 [25] Reza K M, Kurny A S W, Gulshan F (2017) Parameters affecting the photocatalytic
629 degradation of dyes using TiO_2: a review. Appl. Water Sci. 7:1569–1578

630 [26] Abdellah M H, Nosier S A, El-shazly A H, Mubarak A A (2018) Photocatalytic
631 decolorization of methylene blue using TiO_2/UV system enhanced by air sparging.
632 Alex. Eng. J. 57:3727–3735

633 [27] Soltani N, Saion E, Hussein M Z, Erfani M, Abedini A, Bahmanrokh G, Navasery
634 M, Vaziri P (2012) Visible light-induced degradation of methylene blue in the
635 presence of photocatalytic ZnS and CdS nanoparticles. Int. J. Mol. Sci., 13:12242–
636 12258

637 [28] Gajbhiye S B (2012) Photocatalytic degradation study of methylene blue solutions
638 and its application to dye industry effluent. IJMER 2:1204–1208

639 [29] Okamoto K, Yamamoto Y, Tanaka H, Tanaka M, Itaya A (1985) Heterogeneous
640 Photocatalytic Decomposition of Phenol over TiO_2 Powder. Bull. Chem. Soc. Jpn.
641 58: 2015-2022

642 [30] Al-Sayyed G, D'Oliveira J, Pichat P (1991) Semiconductor-sensitized
643   photodegradation of 4-chlorophenol in water. J. Photochem. Photobiol. A: Chem. 58:
644   99–114

645 [31] Hu Q, Liu B, Zhang Z, Song M, Zhao X (2014) Temperature effect on the
646   photoeatalytic degradation of methyl orange under UV-vis Light irradiation. Journal
647   of Wuhan University of Technology-Mater. Sci. Ed. 25:210-213

648 [32] Kaur J, Bansal S, Singhal S (2013) Photocatalytic degradation of methyl orange
649   using ZnO nanopowders synthesized via thermal decomposition of oxalate precursor
650   method. Physica, B Condens. Matter 416:33–38

651 [33] Tang Z W, Huang C P (1995) Inhibitory Effect of Thioacetamide on CdS
652   Dissolution During Photocatalytic Oxidation of 2, 4-Dichlorophenol. Chemospher
653   30:1385–1399
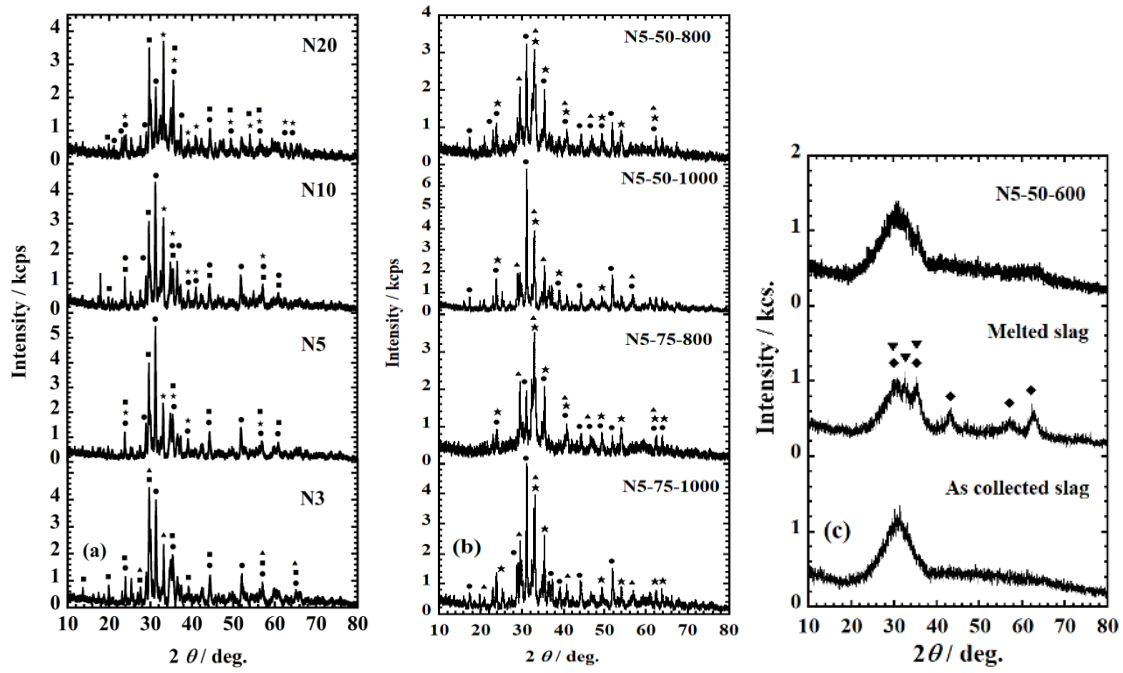
654

655

656

657

658

659

660

661

662

663

664

665

Slag + **(13M) HNO₃** 1 (g): **20, 10, 5 and 3** (ml)	Slag + **(13M) HNO₃ + DW**
Stirring at RT	**Stirring at RT 6 h**
Dissolved slag solution	**Dissolved slag solution**
Drying at 80°C – 24 h	**Drying at 80°C – 24h**
Heat treatment at 1000°C -100 min	**HT at 1000, 800 °C -100 min**
HT samples	**HT samples (1-5-75 -800 / 1000)** **HT samples (1-5-50 -800 / 1000)**
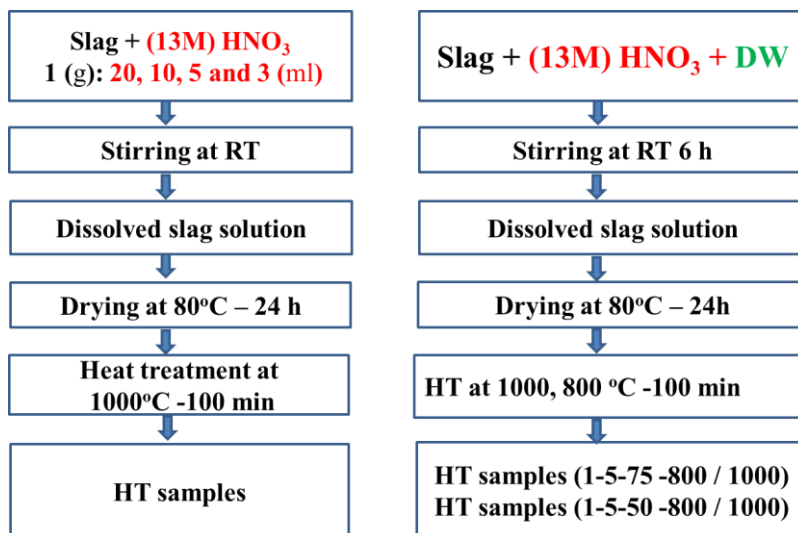
666
667
668
669
670
671
672
673
674
675
676
677
678
679
680
681
682
683
684   A. S. Ali *et al.*, Scheme 1
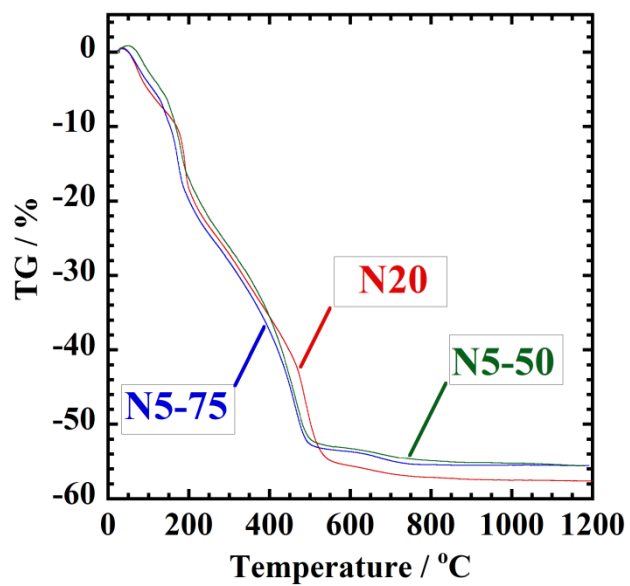
685
686
687
688
689
690
691
692
693
694
695
696
697
698
699
700
701   A. S. Ali *et al.*, Fig. 1

702
703
704
705
706

● Gehlenite	▲ Andradite
■ Essenite	◆ Iron silicon oxide
★ α-Fe$_2$O$_3$ (Hematite)	▼ Calcium silicate

707
708
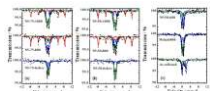709
710
711
712
713
714
715
716
717   A. S. Ali *et al.*, Fig. 2 (a), (b), (c)
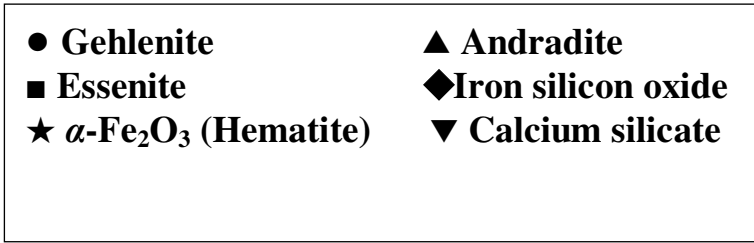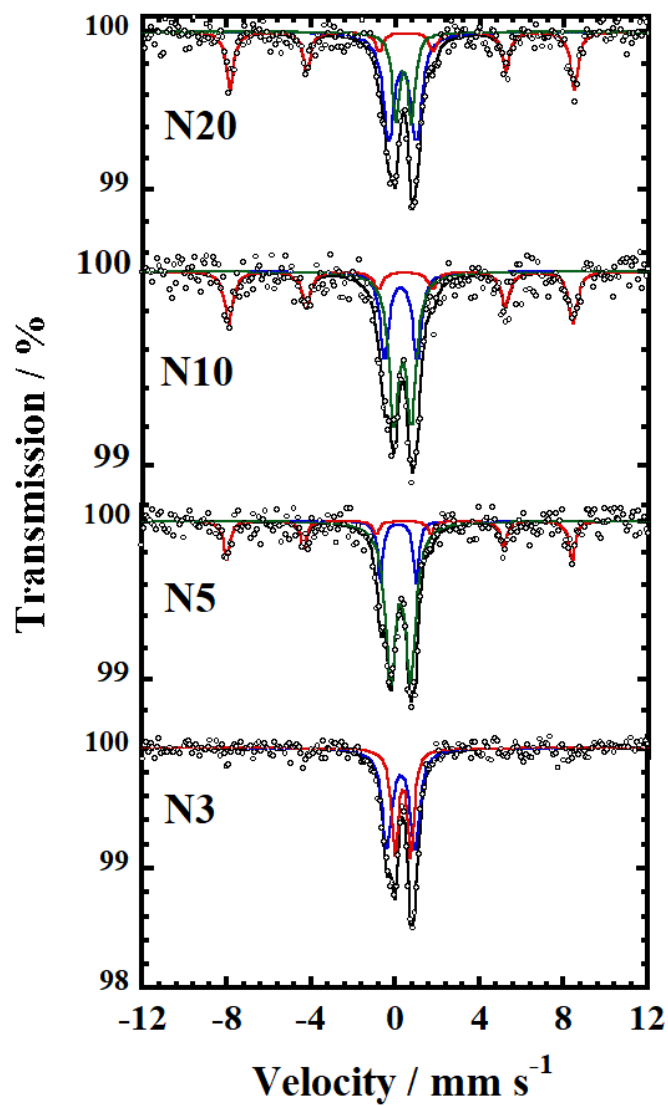
718
719
720
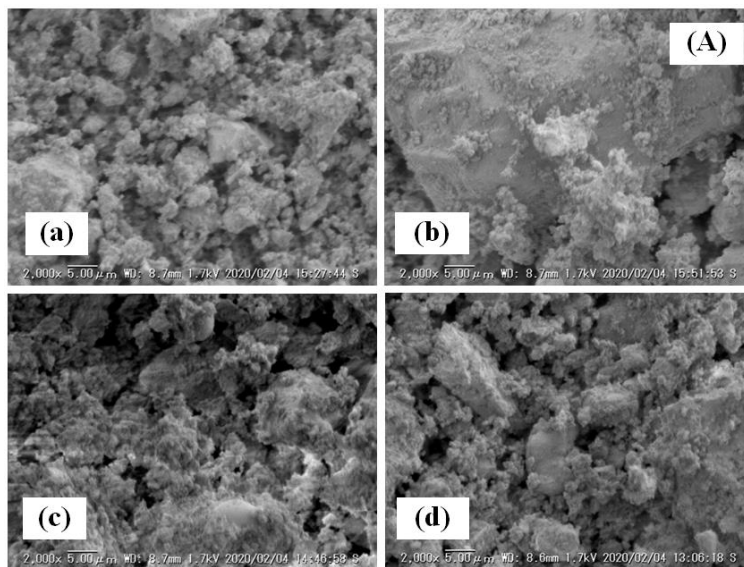721
722
723
724
725
726
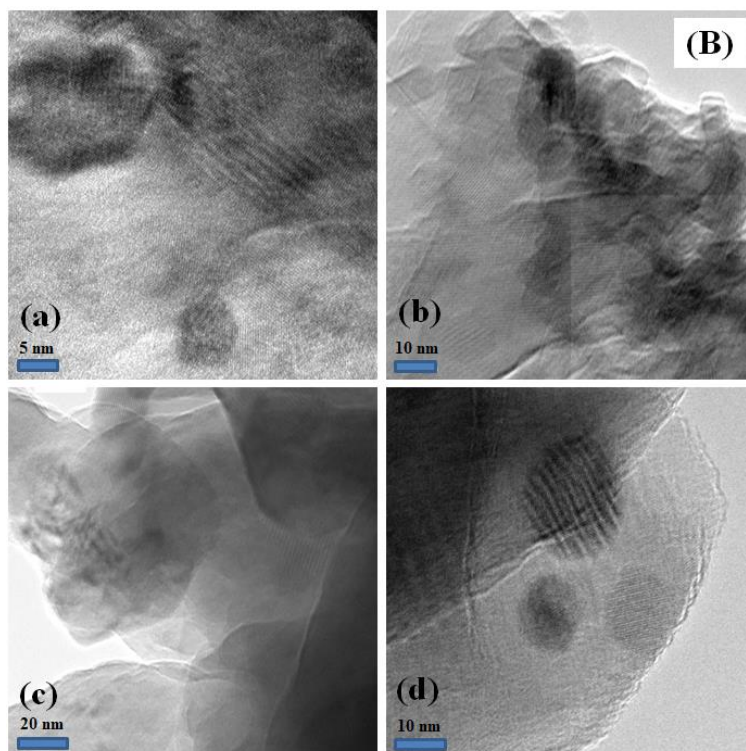727   A. S. Ali *et al.*, Fig. 3
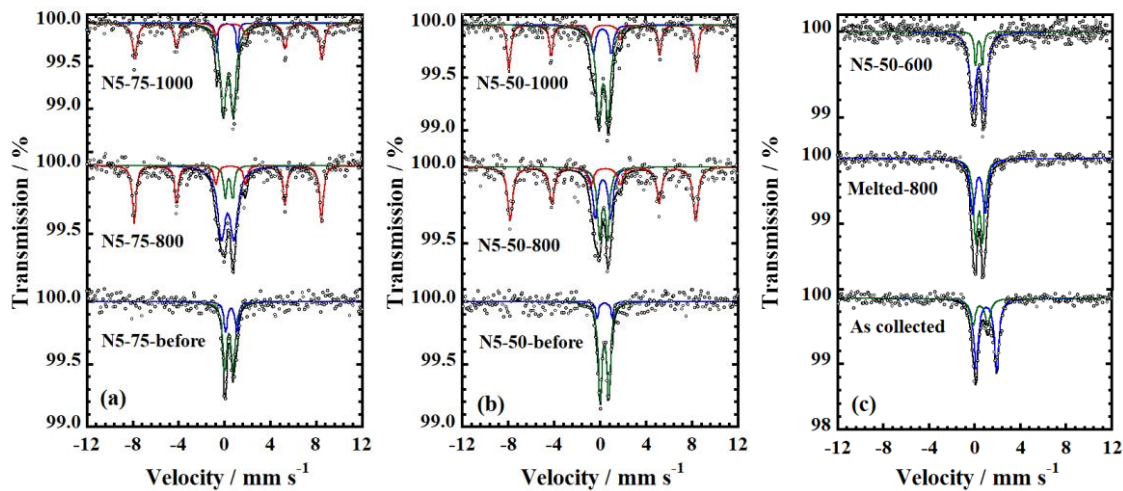
728
729

730
731
732
733
734
735
736
737
738
739
740
741
742
743
744
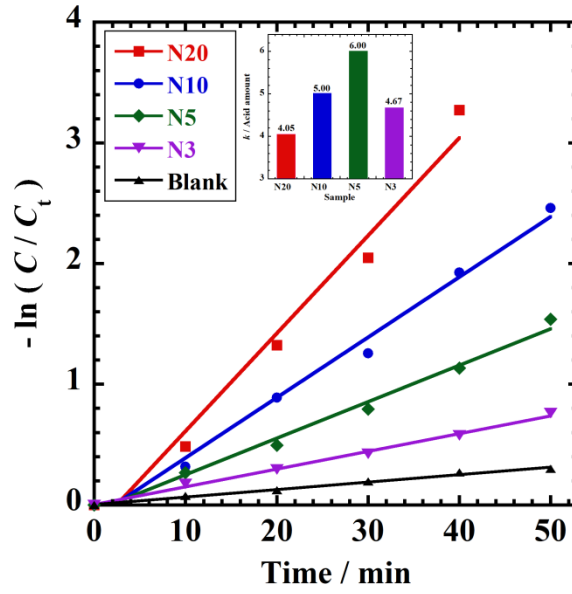745
746   A. S. Ali *et al.*, Fig. 4 (a), (b), (c)
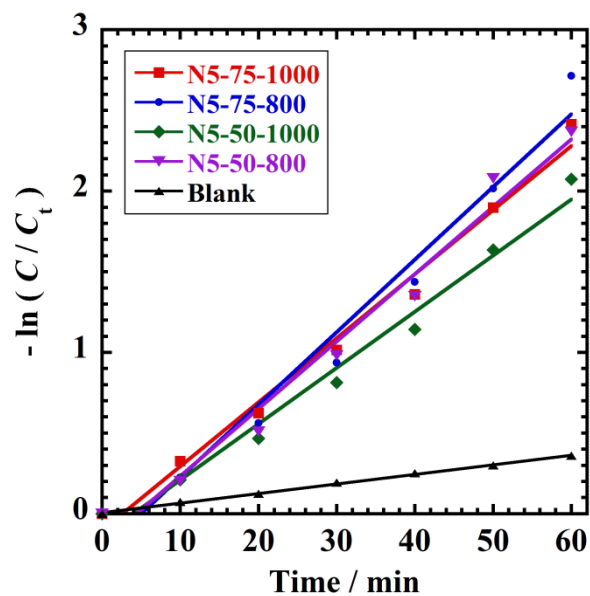
747
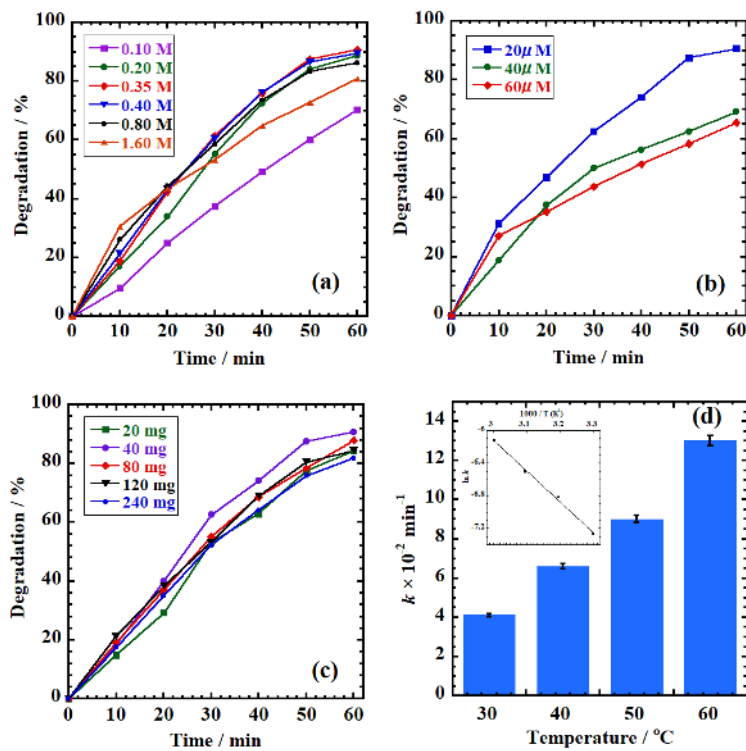
748
749

750

751

752   A. S. Ali *et al.*, Fig. 5

753
754
755
756
757
758
759
760
761
762
763
764
765
766
767
768
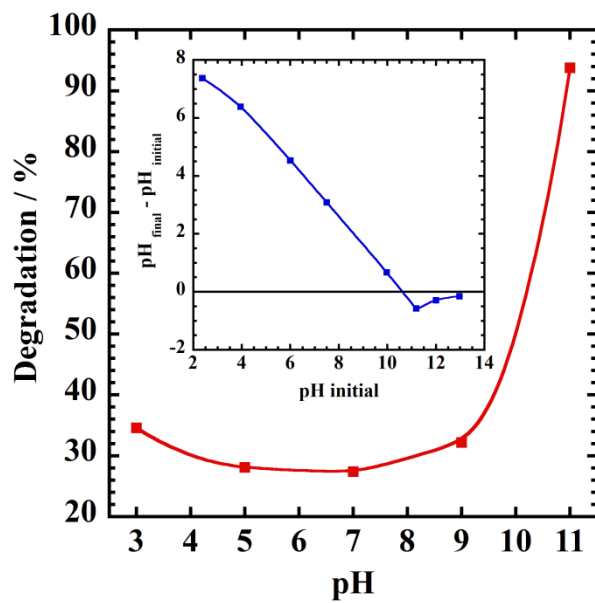769   A. S. Ali *et al.*, Fig. 6

770

771
772
773
774
775
776
777
778
779
780
781
782
783
784
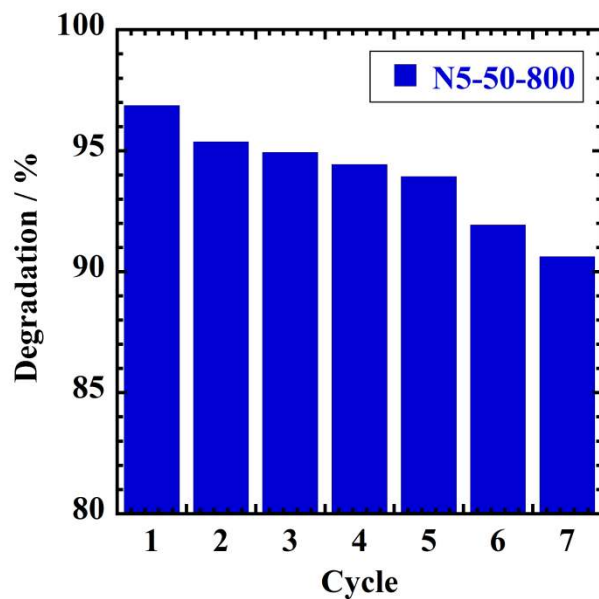785
786   A. S. Ali *et al.*, Fig. 7

787
788
789
790
791
792
793
794
795
796
797
798
799
800
801   A. S. Ali *et al.*, Fig. 8 (a), (b), (c), (d)

802
803
804
805
806
807
808
809
810
811
812
813
814
815
816
817
818   A. S. Ali *et al.*, Fig. 9

819
820
821
822
823
824
825
826
827
828
829
830
831
832
833
834
835   A. S. Ali *et al.*, Fig. 10

Figure Captions

837   **Scheme 1** Schematic diagram of the sample preparation using concentrated HNO_3 (left)

838   and diluted HNO_3 (right)

839   **Fig. 1** TG curves of the samples N20, N5-75 and N5-50

840   **Fig. 2** XRD patterns of samples (a) prepared using concentrated HNO_3 heat-treated at

841   1000 °C for 100 min, (b) prepared using diluted HNO_3 heat-treated at 800 and 1000 °C

842 for 100 min and (c) as collected slag, melted slag heat-treated at 800 °C for 100 min and

843 the sample prepared using diluted HNO_3 heat-treated at 600 °C for 100 min

844

845 **Fig. 3** RT Mössbauer spectra of samples prepared using concentrated HNO_3 heat-treated

846 at 1000 °C for 100 min

847

848 **Fig. 4** RT Mössbauer spectra of samples prepared using diluted HNO_3 (a) 75% (b) 50%

849 and (c) as collected slag, melted slag heat-treated at 800 °C for 100 min and the sample

850 prepared using diluted HNO_3 heat-treated at 600 °C for 100 min

851

852 **Fig. 5** Images of (A) SEM and (B) TEM of the samples (a) N5-75-800 (b) N5-75-1000

853 (c) N5-50-800 (d) N5-50-1000

854

855 **Fig. 6** Kinetic dye degradation measurements of methylene blue for the samples prepared

856 using concentrated HNO_3 heat-treated at 1000 °C for 100 min under photo Fenton the

857 inset is the ratio of k and acid amount for each sample

858

859 **Fig. 7** Kinetic dye degradation measurements of methylene blue for the samples prepared

860 using diluted HNO_3 heat-treated at 800 and 1000 °C for 100 min under photo Fenton

861

862 **Fig. 8** Effect of (a) H_2O_2 concentration, (b) MB concentration, (c) catalyst (iron silicate

863 powder) loading and (d) temperature on the MB degradation for the sample N5-50 heat-

864 treated at 800 °C for 100 min

865

866 **Fig. 9** Influence of pH on the MB degradation for the sample N5-50 heat-treated at 800

867 °C for 100 min the inset is zero point of charge

868

869 **Fig. 10** Reusability of the samples N5-50-800 for MB degradation at pH 11 under

870 catalyst loading 4 g/L, MB concentration 20 μM and H_2O_2 concentration 0.35M

871
872

873 **Table 1** XRF compositional analysis of domestic waste slag (weight %) collected July
874 2018

$_3$	Fe_2O_3	CaO	Na_2O	TiO_2	MgO	P_2O_5	K_2O	
0	18.33	24.61	4.69	2.14	3.12	1.45	0.21	

875
876
877
878
879
880
881
882
883
884
885
886
887
888
889
890
891
892
893
894
895
896
897
898 A. S. Ali *et al*
899 **Table 2** Composition and identification of the samples dissolved in diluted HNO_3

Slag (g)	HNO_3 (ml)	DW (ml)	HNO_3 V (%)	Sample identification (Slag-Solution-HNO_3)
1.00	3.75	1.25	75	1-5-75
1.00	2.50	2.50	50	1-5-50
1.00	1.25	3.75	25	1-5-25

900
901
902
903
904
905
906
907
908
909

910
911
912
913
914
915
916
917
918
919
920
921 A. S. Ali *et al*

922 **Table 3** Room temperature ^{57}Fe Mössbauer fitted parameters for room temperature
923 analyses of as collected slag (not heat treated), slag melted at 1400 °C; heat treated at
924 800°C for 100 min; and concentrated HNO_3 dissolved slag samples after heat treatment at
925 1000°C for 100 min

Sample	Species	A (%)	δ (mm s^{-1})	Δ (mm s^{-1})	H_{int} (T)	Γ (mm s^{-1})
N20	$Fe^{III}T_d$	44	$0.33_{\pm 0.02}$	$1.30_{\pm 0.10}$	-	$0.63_{\pm 0.05}$
	$Fe^{III}O_h$	23	$0.39_{\pm 0.02}$	$0.74_{\pm 0.06}$	-	$0.40_{\pm 0.09}$
	Hem	33	$0.42_{\pm 0.02}$	$-0.20_{\pm 0.03}$	$50.6_{\pm 0.1}$	$0.42_{\pm 0.05}$
N10	$Fe^{III}T_d$	25	$0.25_{\pm 0.03}$	$1.55_{\pm 0.16}$	-	$0.48_{\pm 0.17}$
	$Fe^{III}T_d$	46	$0.34_{\pm 0.03}$	$0.82_{\pm 0.12}$	-	$0.56_{\pm 0.10}$
	Hem	29	$0.37_{\pm 0.02}$	$-0.23_{\pm 0.05}$	$50.6_{\pm 0.17}$	$0.48_{\pm 0.08}$
N5	$Fe^{III}T_d$	13.7	$0.15_{\pm 0.02}$	$1.69_{\pm 0.04}$	-	$0.29_{\pm 0.07}$
	$Fe^{III}T_d$	66	$0.26_{\pm 0.01}$	$0.95_{\pm 0.03}$	-	$0.58_{\pm 0.03}$
	Hem	20.3	$0.35_{\pm 0.03}$	$-0.21_{\pm 0.05}$	$50.7_{\pm 0.2}$	$0.35_{\pm 0.08}$
N3	$Fe^{III}T_d$	57.5	$0.29_{\pm 0.01}$	$1.33_{\pm 0.04}$	-	$0.53_{\pm 0.13}$
	$Fe^{III}O_h$	42.5	$0.38_{\pm 0.01}$	$0.76_{\pm 0.02}$	-	$0.37_{\pm 0.03}$
Melted slag	$Fe^{III}O_h$	55.6	$0.36_{\pm 0.01}$	$0.62_{\pm 0.06}$	-	$0.44_{\pm 0.05}$
	$Fe^{III}T_d$	44.4	$0.34_{\pm 0.01}$	$1.10_{\pm 0.09}$	-	$0.51_{\pm 0.06}$
As collected slag	$Fe^{II}O_h$	70.2	$1.01_{\pm 0.01}$	$1.81_{\pm 0.02}$	-	$0.47_{\pm 0.03}$
	$Fe^{III}O_h$	29.8	$0.48_{\pm 0.06}$	$1.32_{\pm 0.09}$	-	$0.53_{\pm 0.09}$

926 *Hem.* Hematite, T_d tetrahedral, O_h octahedral, A absorption area, δ isomer shift, Δ
927 quadrupole splitting, H_{int} internal magnetic field, Γ line width
928

929
930
931
932
933
934
935 A. S. Ali *et al*

936 **Table 4** Room temperature ^{57}Fe Mössbauer fitted parameters for room temperature
937 analyses of diluted HNO_3 dissolved slag samples before and after heat treatment at 600,
938 800 and 1000°C for 100 min

Sample	Species	A (%)	δ (mm s^{-1})	Δ (mm s^{-1})	H_{int} (T)	Γ (mm s^{-1})
N5-50-1000	Fe^{III} T_d	13.6	0.24 ± 0.01	1.58 ± 0.06	-	0.46 ± 0.07
	Fe^{III} T_h	52.4	0.32 ± 0.01	0.80 ± 0.02	-	0.56 ± 0.04
	Hem	34.0	0.37 ± 0.01	−0.23 ± 0.03	50.7 ± 0.1	0.35 ± 0.04
N5-50-800	Fe^{III} T_d	23.4	0.28 ± 0.03	1.36 ± 0.1	-	0.52 ± 0.1
	Fe^{III} T_d	27.0	0.32 ± 0.02	0.69 ± 0.08	-	0.45 ± 0.08
	Hem	49.6	0.39 ± 0.02	−0.23 ± 0.04	50.1 ± 0.1	0.53 ± 0.07
N5-50-600	Fe^{III} T_d	84.0	0.32 ± 0.01	1.04 ± 0.06	-	0.58 ± 0.03
	Fe^{III} O_h	16.0	0.35 ± 0.02	0.62 ± 0.05	-	0.25 ± 0.08
N5-50-bef	Fe^{III} O_h	88.7	0.36 ± 0.01	0.74 ± 0.04	-	0.38 ± 0.04
	Fe^{III} O_h	10.3	0.39 ± 0.05	1.32 ± 0.14	-	0.27 ± 0.03
N5-75-1000	Fe^{III} T_d	7.1	0.20 ± 0.02	1.81 ± 0.06	-	0.22 ± 0.08
	Fe^{III} T_d	54.5	0.30 ± 0.01	0.88 ± 0.03	-	0.60 ± 0.04
	Hem	38.3	0.43 ± 0.02	−0.22 ± 0.03	50.6 ± 0.10	0.48 ± 0.06
N5-75-800	Fe^{III} O_h	9.9	0.36 ± 0.04	0.65 ± 0.06	-	0.33 ± 0.10
	Fe^{III} T_d	50.3	0.26 ± 0.02	1.10 ± 0.10	-	0.81 ± 0.06
	Hem	39.8	0.39 ± 0.01	−0.25 ± 0.02	50.6 ± 0.07	0.38 ± 0.03
N5-75-bef	Fe^{III} O_h	72.4	0.37 ± 0.02	0.73 ± 0.04	-	0.40 ± 0.05
	Fe^{III} O_h	27.6	0.57 ± 0.04	0.97 ± 0.08	-	0.34 ± 0.1

939 *Hem.* Hematite, T_d tetrahedral, O_h octahedral, A absorption area, δ isomer shift, Δ
940 quadrupole splitting, H_{int} internal magnetic field, Γ line width
941
942

943
944
945
946 A. S. Ali *et al*
947 **Table 5** Surface area and *k* values of the samples prepared using diluted HNO_3 and heat
948 treated at 800 and 1000 $^{\circ}$C for 100 min

Sample	Surface area (m^2 / g)	k ($\times 10^{-2}$ min^{-1})
N5-50-800	2.63 ± 0.05	4.1 ± 0.1
N5-50-1000	2.16 ± 0.05	3.4 ± 0.1
N5-75-800	5.38 ± 0.10	4.5 ± 0.1
N5-75-1000	3.64 ± 0.07	3.9 ± 0.1

949
950
951
952
953
954
955
956
957
958
959
960
961
962
963
964
965
966
967
968
969
970 A. S. Ali *et al*
971